

**IMPULSE COUPLING TO TARGETS IN VACUUM
BY KrF, HF AND CO₂ SINGLE-PULSE LASERS**

C. R. Phipps, Jr., T. P. Turner, R. F. Harrison, G. W. York, W. Z. Osborne,*
G. K. Anderson, X. F. Corlis, L. C. Haynes, H. S. Steele and K. C. Spicochi†

Los Alamos National Laboratory
Chemical and Laser Sciences Division
Mail Stop J566
Los Alamos, New Mexico 87545

and

T. R. King,
Boeing Aerospace Company
Physical Sciences Research Center
Mail Stop 2R-00
P.O. Box 3999
Seattle, WA 98124

ABSTRACT

We present a laser-target scaling model which permits approximate prediction of the dependence of ablation pressure, mechanical coupling coefficient, and related parameters in vacuum upon single-pulse laser intensity (I), wavelength (λ) and pulsewidth (τ) over extremely broad ranges. We show that existing data for vacuum mechanical coupling coefficient for metallic and endothermic non-metallic, surface-absorbing planar targets follows this empirical trend to within a factor-of-2 over 7 orders of magnitude in the product ($I \lambda \sqrt{\tau}$). The comparison we present is valid for intensity equal to or greater than the peak-coupling intensity, I_{\max} , where dense

*Deceased.

†Parts of this work were supported by SDIO/T/KE, DARPA, and ARDEC.
plasma formation mediates laser-target coupling. Mechanical coupling coefficients studied ranged over 2 orders of magnitude.

The data supporting this trend represent intensities from 3 MW/cm² to 70 TW/cm²,

pulsewidths from 1.5 ms to 500 ps, wavelengths from 10.6 μm to 248 nm and pulse energies from 100 mJ to 10 kJ. With few exceptions, data approximating 1-dimensional or planar expansions were selected.

Previously, meaningful scaling of ablation pressure parameters with I , λ , τ was not possible because existing data concentrated in a small range of these parameters. Our own data, obtained in the low- and mid-range of $(I\lambda\sqrt{\tau})$, completes the experimental picture. Since this new data was derived from 5 separate experiments with specialized character and purpose, detailed accounts of this work will appear separately. In this paper, we summarize the experimental conditions and select only those data which are relevant to the scaling issue. We find that laboratory-scale laser experiments can often give impulse coupling data which agree with results from much higher energy experiments without much error, and at much lower cost.

We review a theory of vacuum laser ablation, specialize it to a quantitative description of mechanical coupling, and show that the resulting model provides a simple physical description which comes quite close to the observed empirical trend. This is accomplished with minor elaborations of the theory as originally presented to account for the temperature-dependence of plasma ionization states, while adhering to the premise that a simple and generally applicable treatment of laser impulse production should be available.

The theoretical model can quantitatively predict vacuum ablation pressure for opaque targets without adjustable parameters to the factor-of-2 accuracy in which we are interested. Other published scaling models omit one or more of the important variables, lack broad applicability or deviate more noticeably from the observed trend.

INTRODUCTION

When a laser pulse is incident on a target in vacuum, mechanical impulse is produced by the pressure of photoablation at the target surface. By convention, the figure of merit for this interaction is the mechanical coupling coefficient C_m :

$$C_m = p_a/I = J/W_L \quad [1]$$

where p_a is the ablation pressure (dyne/cm²), I is the incident laser intensity (W/cm²), J is the total momentum imparted to the target (dyne-sec) and W_L is the laser energy (J). Units of C_m are dyne/W or dyne-sec/J. Since typical values of C_m are of order 1 - 10, the portion contributed by light pressure is usually very small. Even total reflection gives a photon coupling coefficient $C'_m = 2/c = 6.7 \times 10^{-4}$ dyne/W.

Since the ratio of impulse to energy varies as the reciprocal of the average ablation ejecta velocity [if most of the laser energy is converted to ejecta kinetic energy], minimum ejecta velocity maximizes C_m .

Apart from the high-intensity, short-pulse laser fusion work, only a minority of the published measurements of p_a vs I or of C_m are in vacuum, despite the importance of such measurements at longer pulsewidths and lower intensities. Our work in this area provided the data required to complete an accurate picture of the variation of ablation pressure with intensity and other laser parameters for the first time. Experiments in an ambient gas background above about 1 torr pressure usually operate in a quite different physical regime¹ in which, as with radiometers, the reaction of the ambient gas to the heated target is important. We only consider this regime incidentally.

Interest in an approximate model for predicting optimum photoablation parameters goes back to the earliest days of laser fusion studies,² and is motivated by the immense parameter space available with pulsed laser sources. The issue of laser-target interactions is further complicated when the range of photophysical properties of target materials is considered.

It is apparent, for example, that if laser light is absorbed in-depth in a semi-opaque material, mechanical coupling can be more efficient than with surface absorption. This is because the laser energy is then employed mainly to accelerate cold mass

fragments, without having to vaporize the entire ejected mass. Photolytic³ and exothermic target behavior are other possibilities.

To limit attention to a tractable problem, giving hope of a simple, broadly applicable scaling model, we avoid considering regimes where material properties play a major role. We consider only endothermic surface absorbers, using as a criterion:

$$x_{th} \gg 1/\alpha \quad [2]$$

where
$$x_{th} = 0.969 \sqrt{\kappa\tau} \quad [3]$$

is the heated layer thickness at the end of the laser pulse,⁴ κ is the thermal diffusivity of the material and $1/\alpha$ is the laser absorption depth. This restriction includes all metals and many C-H-type materials in the uv-to-ir wavelength range considered here.

More importantly, we restrict attention to the intensity range (for a particular laser-target interaction) lying at or above the intensity at which peak coupling occurs. Gregg and Thomas⁵ were the first to note that C_m in vacuum rapidly reached a maximum at an intensity I_{max} , thereafter declining with increasing intensity according to

$$C_m = \Gamma (I/I_{max})^{-n} \quad [4]$$

for a given wavelength and pulse duration.

Figure 1 shows typical data from our own work⁶ illustrating this behavior for a KrF laser coupling to nylon, where $I_{max} = 2 \times 10^8$ W/cm². In this instance, the best-fit trend line for data $I > I_{max}$ gave $n = -0.36$ and $\Gamma = 6.8$ dyne/W. Scatter, expressed as standard deviation of the spread of the data relative to the best-fit trend line was $\pm 8\%$.

In the Gregg and Thomas measurements, with a 7.5-ns ruby laser on 5 metals and graphite, Γ averaged 7.0 dyne/W, $I_{max} \approx 6.5 \times 10^8$ W/cm² and the index n had a value 0.288 ± 0.05 . This behavior is due to the ignition of dense plasma in the vapor close to the target surface which mediates the coupling of laser energy to the material for $I \geq I_{max}$. In this "asymptotic" regime, to the approximation in which we are interested here, the specific material properties of the targets we consider enter only as plasma parameters, e.g., the ratio $(A/2Z)$ of atomic mass number to average ionization charge

state in the ablation vapor. Because the intensity range from the onset of vaporization to I_{\max} is so small and, therefore, difficult to maintain, this restriction excludes only a limited range of practical behavior from our study. This excluded range is an appropriate subject for more complex theories treating specific materials and laser parameters^{7,8} with greater accuracy than does the present scaling model.

In order to minimize the further complication of "dimensionality" in our theory, and because it is a weak effect empirically, we limit discussion mainly to the regime in which the expansion associated with photoablation is called "one-dimensional".

In fact, no laser-target interaction is truly planar. Plasma from flat targets irradiated by finite-size laser beams in vacuum expands longitudinally and laterally, the expansion becoming physically significant when a characteristic dimension of the interaction region becomes comparable to the laser spot diameter.

One such characteristic dimension is the distance x_0 which separates the target ablation surface from the region near the critical density surface where laser energy is absorbed via inverse bremsstrahlung. This distance is⁹

$$x_0 = 0.1 I^{4/3} \lambda^{14/3} \text{ cm} \quad [5]$$

For example, for planar targets, the numerics of Eq. [5] indicate that laser spots larger than about 50 μm for 1- μm wavelength and laser fusion intensities ($I = 10 \text{ TW}/\text{cm}^2$), 0.1 \AA for KrF lasers and $I \leq 10 \text{ GW}/\text{cm}^2$, and 300 μm for CO_2 lasers in the same intensity range represent one-dimensional experiments by this criterion. These parameter ranges safely include our data which will be reported here.

Different dimensionality considerations can arise from transverse electron thermal conduction, and from lateral motion of the plasma in the typical experimental situation where target illumination is nonuniform. When these effects become significant, energy and momentum transfer to the target occur over a larger area, and the geometry of laser absorption changes during the pulse, complicating data analysis.

It will be shown in the third section following that plasma motion is the main effect for the experiments we consider, and that a practical criterion for assessing this is:

$$D_t = 2c_a\tau \ll D \text{ (1-dimensional)} \quad [6]$$

where D is the laser spot diameter and c_a is the sound speed, usually 1-10 cm/ μ s in these experiments. For the purposes of this approximate criterion, the ablation pressure pulse duration τ_p and the laser pulse duration τ_L are taken to be similar.

When we quote data taken outside this limit, it will be (except in one case) because the effects of departure from one-dimensional expansion are expected to be small, or to demonstrate the small magnitude of the correction. We will, however, summarize the theoretical predictions concerning dimensionality.

For the regime we have defined, a large number of theoretical models have been presented, of which references 9-21 are a selection. The model we discuss as best representing experimental observations of the dependence of ablation pressure p_a on the variables I , λ and τ was developed independently by Caruso,^{10,14} Nemchinov¹¹ and Kidder.¹³ It was further elaborated by Kidder at the Varenna meeting¹⁵ in a concise, computationally useful form. Caruso and Nemchinov treat one-dimensional and two-dimensional laser-target interactions in the subcritical regime, where

$$\rho_a < \rho_c = (Am_p/Z) n_{ec} \quad [7]$$

In Eq. [7], ρ_a is the ablation mass density, A is ion mass in atomic mass units, m_p is the proton mass, and n_{ec} is the critical electron density, given by

$$n_{ec} = 1.115 \times 10^{13}/\lambda^2 \text{ cm}^{-3} \quad [8]$$

They do not, however, treat the critical pressure regime. Kidder studies 1-dimensional expansions in both pressure regimes, with careful attention to the transition between the two (generally at an early time in high-intensity interactions), but gives only cursory attention to two-dimensional hydrodynamics.

Where these 3 theories overlap, they predict the same scaling behavior, and collectively give a complete treatment of the subject, insofar as a generic model can describe the wide variety of conditions observable in vacuum laser-target interactions.

This model has sometimes been called the Basov model, but it is important to realize that Basov¹² based his development on Nemchinov's theory, and neglected to give the dependence of pressure on wavelength, instead stating an absorption coefficient specialized to the 1.06- μm case. Krokhin¹⁶ presented a model similar to Caruso-Nemchinov-Kidder at the Varenna meeting, and Puell¹⁹ later obtained the same two-dimensional and critical pressure results by somewhat different methods. Bobin¹⁶ and Fauquinon¹⁷ obtained only the result for the critical pressure, and Jarboe²⁰ quotes their result, adducing experimental data to justify this scaling relation in a short-pulse ruby laser experiment. Max²¹ considered a special case of two-dimensional flow with inhibited electron thermal conduction, obtaining substantially different dependences from the other authors.

The principal results of Caruso-Nemchinov-Kidder (C-N-K) are the following:

$$\text{1-D expansion, } p_a < p_c: \quad p_a \propto I^{3/4} \lambda^{-1/4} \tau^{-1/8} \quad [9]$$

$$\text{2-D expansion, } p_a < p_c: \quad p_a \propto I^{7/9} \lambda^{-2/9} D_s^{-1/9} \quad [10]$$

$$\text{1-D expansion, } p_a = p_c: \quad p_a \propto I^{2/3} \lambda^{-2/3} \quad [11]$$

Eq. [10] is the only specific allusion we will make to the theory of 2-D interactions in this paper. We note that the predicted effect of the 2-D regime is to change the exponent of the intensity dependence of p_a from 0.75 to 0.78, that of the wavelength dependence from 0.25 to 0.22, and to replace the time variation with $\tau = D_s/c_a$ in the time-dependent, one-dimensional expression for c_a and p_a , resulting in a very weak dependence on D_s . It is seen that laser spot sizes ranging from 1 mm to 10 cm change the ablation pressure by a factor of only 1.7 in this model.

In the next section, we will follow Kidder's approach in outlining the derivation of the one-dimensional results [9] and [11] for p_a , and extend this to the behavior of other variables of interest for laser-target interaction work.

It will be seen that the behavior of $C_m = p_a/I$ corresponding to Eqs. [9] and [11] is:

$$\text{1-D subcritical expansion: } C_m \propto (I\lambda\sqrt{\tau})^{-1/4} \quad [12]$$

$$\text{1-D critical expansion: } C_m \propto (I\lambda^2)^{-1/3} \quad [13]$$

While it may seem that the substantial differences in parametric behavior expressed by Eqs. [12] and [13] could be easily resolved by experiment, the situation is not so simple as it appears. Data from a single experiment often cover a limited range of I and no range in λ and τ . Attempts to correlate results from different experiments are subject to the fact that much of the short-wavelength data comes from short-pulse lasers, and long-wavelength data from long-pulse lasers, so that it has not been easy to isolate wavelength- from pulsewidth-dependence in scaling. Further, it is essential in such a scaling comparison to use data from similar materials and experimental conditions, substantially restricting the amount of relevant data.

To resolve these difficulties, we separately compare data from carbon and C-H type materials and from aluminum alloy targets. In both cases, our own data, representing low- and mid-range values of $(I\lambda\sqrt{\tau})$, provide a crucial counterweight to existing laser fusion data at high values of $(I\lambda\sqrt{\tau})$, to facilitate an accurate, empirical scaling comparison. We have included some very long pulse data from other authors, also at low values of $(I\lambda\sqrt{\tau})$ to eliminate confusion between λ and τ as variables.

We find that the experimental data closely fits the scaling predicted by Eqs. [12] and [13], but with an exponent of -0.30 rather than -0.25. We explain this discrepancy as due to variation of a temperature dependent parameter in the model.

THEORY

In the asymptotic intensity range $I > I_{\max}$, vacuum impulse generation by pulsed lasers is properly a plasma physics phenomenon. In this region, the incident radiation is no longer transmitted directly to the solid surface but is absorbed in a thin layer near the critical density [Eq. 8] and reradiated or scattered, ultimately reaching the target or escaping into vacuum. The optical depth of this layer normally depends only weakly on intensity, reaching a constant, "self-regulating" value on the order of unity.^{15,16,22} This approximation only breaks down at or near the plasma threshold where very large

coupling can be observed which does depend on detailed material properties.

A review of existing data and models^{5,7-8, 22-26} reveals that the intensity I_p at which vacuum plasma ignition occurs is closely related to and slightly less than the intensity I_{\max} for which maximum C_m is observed. For metallic targets in vacuum and laser pulses of duration $10^{-8} < \tau < 10^{-3}$ s,

$$I_{\max} \sqrt{\tau} = B_{\max} \quad [14]$$

$B_{\max} \approx 8 \times 10^4 \text{ W } \sqrt{\text{s}}/\text{cm}^2$ describes the trend of experimental literature for aluminum alloys in this pulse-width range, with data for other metals lying slightly above or below this trend. No strong dependence on laser wavelength in the range 0.25 to $10.6 \mu\text{m}$ is noted [Fig. 2]. We remark that reference 7 predicts

$$I_p \sqrt{\tau} = B_p \quad [15]$$

with $B_p = 4.5 \times 10^4 \text{ W } \sqrt{\text{s}}/\text{cm}^2$ for aluminum at $0.35 \mu\text{m}$, 56% of the empirical B_{\max} .

Scatter between our own experimental results for B_{\max} with aluminum^{6,24,25} and existing data amounts to about a factor of 2, due to incompleteness of existing data, plotting average vs. peak intensity, or other causes.

For intensities we consider, inverse bremsstrahlung is the dominant plasma heating mechanism. The absorption coefficient for this process is given by:^{15,27}

$$\alpha = (4/3)(2\pi/3kT_e)^{1/2} n_e n_i Z^2 e^6 g_{\text{ff}} [1 - \exp(-h\nu/kT_e)] / h c m_e^{3/2} \nu^3 \quad \text{cm}^{-1} \quad [16]$$

With $h\nu \ll kT_e$ (a good approximation for 10 to 100 eV plasmas and visible to infrared lasers),

$$\alpha \propto [4(2\pi)^{1/2}/3^{3/2}] n_e n_i Z^2 e^6 g_{\text{ff}} / c m_e^{3/2} \nu^2 (kT_e)^{3/2} \quad \text{cm}^{-1} \quad [17]$$

where n_e , T_e and n_i are electron density (cm^{-3}), temperature (K) and ion density, and ν is the laser frequency. The Gaunt factor, g_{ff} , is a quantum-mechanical correction with

magnitude near unity.^{28,29} From charge neutrality ($n_e = Z n_i$) we have:

$$\alpha = 1.97 \times 10^{-23} Z^3 n_i^2 g_{ff} \lambda^2 / T_e^{3/2} \quad \text{cm}^{-1} \quad [18]$$

Since the mass density $\rho_a = (A m_p / Z) n_e$, while the adiabatic sound speed³⁰

$$c_a = [\gamma(Z+1)kT_e / A m_p]^{1/2} \quad \text{cm/s} \quad , \quad [19]$$

The absorption coefficient (Eq. [18]) may be expressed in hydrodynamic variables as:

$$\alpha = \beta \rho_a^2 / c_a^3 \quad \text{cm}^{-1} \quad [20]$$

where

$$\beta = C_1 Z^3 (Z+1)^{3/2} \lambda^2 / A^{7/2} \quad \text{cm}^8 \text{g}^{-2} \text{s}^{-3}. \quad [21]$$

In Eq. [21], $C_1 = 1.136 \times 10^{37}$, with $\gamma = 5/3$ (ideal gas).

The optical thickness of the plasma at the head of the adiabatic rarefaction produced by the laser pulse, is

$$S = \alpha c_a \tau \quad [22]$$

The incident light intensity needed to support the ablation flow is

$$I = \xi \rho_a c_a^3 \quad \text{erg cm}^{-2} \text{s}^{-1} \quad [23]$$

In Eq. [23], $\xi = M (M^2 + 3)/2$, where M is the ablation flow Mach number. Eqs. [20], [22] and [23] may be combined to give expressions for ρ_a and c_a :

$$\rho_a = (S/\beta\tau)^{3/8} (I/\xi)^{1/4} \quad \text{g/cm}^3 \quad [24]$$

$$c_a = (\beta\tau/S)^{1/8} (I/\xi)^{1/4} \quad \text{cm/s} \quad [25]$$

from which the ablation shock pressure may be written:

$$\begin{aligned} p_a &= [(1+\gamma M^2)/\gamma] \rho_a c_a^2 \\ &= [(1+\gamma M^2)/\gamma] [(S/\beta)^{1/8} I^{3/4} / \tau^{1/8} \xi^{3/4} \text{ dyne/cm}^2. \end{aligned} \quad [26]$$

If all the incident light is used to support the ablation, Eq. [26] implicitly includes the variation of p_a with I , λ and τ . The maximum value of p_a occurs when $\rho = \rho_c$ and is:

$$p_c = [(1+\gamma M^2)/\gamma] \rho_c^{1/3} (I/\xi)^{2/3} \quad \text{dyne/cm}^2 \quad . \quad [27]$$

The behavior in Eq. [26] for $p_a < p_c$ corresponds to $p_a = (\tau_1/\tau)^{1/8} p_c$, so that a transition time τ_1 between critical and subcritical pressure may be identified:

$$\tau_1 = S(I/\xi)^{2/3} / \beta p_c^{8/3} \quad \text{s.} \quad [28]$$

After this time τ_1 , a gently time-varying subcritical pressure regime is obtained. It will be found that this subcritical regime includes most of the experimental conditions we treat, notably excepting only short-pulse, long-wavelength experiments.

Invoking self-regulation of the opacity [$S=1$ after $\tau = \tau_1$], the Chapman-Jouguet condition [$M=1$, $\xi=2$], $\gamma = 5/3$, $g_{ff} = 1$, and converting I to W/cm^2 units, we obtain:

$$\tau_1 = 1.05 \times 10^{-4} I^{2/3} A^{5/6} \lambda^{10/3} Z^{-1/3} (Z+1)^{-3/2} \quad \text{s.} \quad [29]$$

Table I gives τ_1 in terms of I for a hydrogenic plasma ($A=Z=1$). Note that τ_1 is a very short interval in most cases, justifying the attention we pay to the subcritical case.

Expressions for pressure, temperature and other variables can be derived using the previous assumptions and practical intensity units, and are listed in Table II.

DISCUSSION

From these relationships emerges the picture of a gently time-dependent density,

pressure, temperature, etc. after a time τ_1 (however short), prior to which time these variables remain fixed at their maximum or minimum critical values, if $I \geq I_p$.

In particular, the important parameter σ (momentum flux), which appears for the first time in Table II, is strictly defined as:

$$\begin{aligned}\sigma(\tau) &= \int_0^{\tau} p_a(t) dt = \rho_c \left[\tau_1 + \int_{\tau_1}^{\tau} (\tau_1/t)^{1/8} dt \right] = \rho_c (\tau_1/\tau)^{1/8} \tau \\ &= \rho_a(\tau) \tau .\end{aligned}\quad [39]$$

The parameters $\psi = A/2Z$ and $\Psi = A/2[Z^2(Z+1)]^{1/3}$ in the Table are near unity for fully-ionized atoms.

The new parameter μ in Eq. [37] for the energy coupling coefficient η (the ratio of target kinetic energy to incident laser energy) is the areal mass density of the target, with units g/cm^2 .

From the point of view of the laser variables, maximum coupling occurs at an intensity approximately predicted by Eq. [14] so that:

$$C_{\max} \cong 0.30 A^{7/16} Z^{-3/8} (Z+1)^{-3/16} \lambda^{-1/4} . \quad [40]$$

This relationship indicates a modest dependence of maximum mechanical coupling in favor of short wavelengths, but independent of pulse duration. For example, in the case of aluminum ($A=27$), Eq. [40] predicts $C_{\max} \cong 16$ for KrF lasers ($\lambda = 0.25 \mu m$), and $C_{\max} \cong 6$ for CO_2 lasers ($\lambda = 10.6 \mu m$). These estimates are about twice what we observed in the two cases. Agreement of this order between experimental results and a simple scaling theory is considered quite good. We do not necessarily claim such good agreement for other variables, such as T_e , in our theory.

Considering the material variables, it will be noted that $C_m = (1+\gamma M^2) / (\gamma \xi c_a) = 8 \times 10^6 / c_a$ in this simple theory, so that anything which acts to reduce the sound speed (high mass density, low intensity) is predicted to improve mechanical coupling.

While C_m has received attention as a figure of merit for analyzing impulse-producing laser-target interactions, we note that the equally important parameter σ is almost linearly proportional to τ , providing the main rationale for using long-pulse lasers to produce momentum remotely in vacuum.

Eqs. [30a] - [35a] suggests using the product $(I\lambda\sqrt{\tau})$ as the principal scaling quantity for rationalizing mechanical coupling data arising in the broad region of laser parameter space where $\tau \geq \tau_1$. Eqs. [30b] - [35b] give the conventional scaling for $\tau < \tau_1$.

LOS ALAMOS EXPERIMENTS

In this section, we summarize several different experiments^{6,24,25} at Los Alamos that produced new data on aluminum and C-H-type materials. The data selected for this report is a subset of all the data obtained in these studies, whose purposes were substantially different and too specialized to discuss in detail in a single paper. To facilitate modeling, the portion selected treats the same target materials - aluminum alloys among metals, and polyethylene, carbon, graphite, graphite epoxy and similar materials among nonmetals. Also, only data for materials which were surface absorbers at the laser wavelength employed was selected.

In the course of this experimental program, 5 different laser systems were employed to obtain the Los Alamos target interaction data. These were: the Kirtland Air Force Base Mjöllnir laser (1.8 μ s, HF), the Los Alamos Gemini laser (1.8 μ s, CO₂), the United Kingdom's Sprite system (40 ns, KrF) and two smaller specially configured, laboratory-scale lasers at Los Alamos (CO₂ and KrF)

Table III summarizes the range of laser parameters (energy, pulsewidth, wavelength, spot diameter, etc.) and other experimental conditions employed in our measurements.

Collectively, these experiments yielded over 2,000 data points for laser-target interactions in vacuum for pulsed laser sources in the ultraviolet through infrared spectrum, over 4 orders of magnitude in target energy and 2 orders in pulse duration, representing small to modest values of $I\lambda\sqrt{\tau}$ (approximately 1 to 1000 W \sqrt{s} /cm).

In order to create a well-prescribed physical situation over the illuminated target surface, it was necessary to arrange uniform target illumination profiles, both in space

and time. In this way, plasma ignition and development could occur uniformly and simultaneously across the target, giving better possibility for a simple scaling theory to represent the interaction. This was more easily accomplished with small than with large laser sources.

In the case of Mjöllnir,²⁵ an M=2, electron-beam-initiated HF unstable resonator system, beam profile on target varied from an approximate replica of the annular pattern characteristic of unstable resonators at the lowest-fluence target position [D=6 cm] to an approximately gaussian shape at best focus [D=1 cm]. A diffraction-limited HF beam with our target illumination f-number of 2.0 would have produced a much smaller, $D \cong 15 \mu\text{m}$ focal spot. Better control of target irradiance profiles would have required system redesign, and so was impractical. The laser output was unpolarized, and occupied a spectrum of about 20 strong lines in the range 2.7 to 3.4 μm .

Beam samples for diagnostics were derived from near-normal-incidence reflections at the wedged target-chamber window, focused with the same convergence used for target illumination. This principle, employed in all our experiments, avoided discrepancies between measured and actual beam distributions due to propagation effects.

Laser fluence on target was adjusted by changing target position relative to beam focus inside the target chamber.

In the case of Gemini,²⁵ a dual, electrically driven CO₂ laser amplifier built for laser fusion, one of the 245-liter, 3-atm final amplifier modules was reconfigured as an M = 2.4 unstable resonator while the second module was set up as a 1- μs master-oscillator-power-amplifier (MOPA), in order to obtain better space and time profiles.

The unstable resonator section produced 2.5 kJ in a 1.8- μs FWHM pulse with the characteristic initial 100-ns "spike" due to gain-switching, comprising 10% of the pulse energy, and a trailing portion 2-3 times smaller in intensity.

The front end driver for the Gemini MOPA²⁴ employed active gain-linewidth narrowing in a pulsed low-pressure gain cell to produce a time-bandwidth-limited 1- μs FWHM pulse (see Fig. 3 and 4). A germanium Faraday rotator³⁰ with 40 dB reverse attenuation prevented parasitic oscillation in this system, and a spark isolator³¹ protected it from amplified retropulse damage (Fig. 5). A standard gas isolator cell³² prevented spontaneous oscillation within the triple-passed Gemini amplifier.

For experiments with the Sprite laser,²⁵ substantial control of beam quality was possible, leading to more reproducible results. Its M=4 KrF unstable resonator achieved 100J output in a 37-ns pulse, 70% of this output confined within a 50 μ r full angle via active injection control.³³ The 100-mJ injection signal was derived from a Lambda-Physik EMG-150 KrF device. An off-axis resonator configuration was employed during our work, giving a 65-mm diameter dark spot at the periphery of the 260-mm-diameter output beam, rather than the usual central obscuration.

Figure 6 is a scanning electron micrograph of the 1-mm diameter crater produced by the Sprite beam focused on a 6061-alloy aluminum target in a typical shot at 0.1 TW/cm². The crater subtended 830 μ r at the target illumination lens in this case, representing effects obtained in the near field of the laser beam. Laser effects on the target cease being observable at 4.5 times the crater diameter, giving qualitative agreement with laser energy distribution measurements.

In the Sprite experiments, beam distribution on target was monitored via photochromic film at the diagnostic beam focal plane, or, when the target was moved beyond focus for lower intensity shots, via a lower-resolution pyroelectric detector array at equivalent positions in the diagnostic beam.

The Los Alamos Optical Physics Laboratory (OPL) laser,²⁴ employed for low-energy 10- μ m target interaction work, consisted of the Fig. 3 master-oscillator driver with output energy augmented to 20 J in two passes through a Lumonics Research Ltd. model 600-A CO₂ amplifier

A demagnified image of a uniformly illuminated hard aperture outside the target chamber produced the target laser irradiance. The Airy-pattern due to the pupil function³⁴ of the target optics dominated this distribution, but only the central portion, whose exp(-2) intensity diameter was typically 1.2 mm, was used to illuminate targets. After beam processing, maximum energy on target was 5 J.

Within the target chamber, a mirror not shown in the figure directed the incident laser beam upward to facilitate measuring impulse via target levitation, as described in the following section.

Qualitatively, the EMG-150 facility⁶ was a duplicate of the OPL 10- μ m experiment for KrF work, except that some target motion relative to best focus was necessary to

augment the range of intensities on target provided by a set of calibrated reflectors (A_1 , A_2 in Fig. 7). The laser was an injection-controlled unstable resonator.

ILLUMINATION UNIFORMITY AND TRANSVERSE THERMAL CONDUCTION

Dimensionality is important because practical laser-target interaction experiments must utilize a finite target and finite, nonuniform target illumination.

When electron thermal conduction is significant, heat can be distributed across the target by illumination intensity gradients at electron sound speeds $c_e \approx \sqrt{Am_p/m_e} \gg c_a$.

In this case, pressure delivered to targets large compared to the central maximum of the illumination distribution will be much lower than might be assumed.

Heat transfer due to electron thermal conduction is given by^{9,28}

$$\mathbf{Q} = K \nabla T \quad \text{W/cm}^2 \quad [41]$$

where $K = 1.95 \times 10^{-11} T_e^{5/2} \delta_T / Z \ln \Lambda \quad \text{W/cm.} \quad [42]$

In Eq. [42], $\ln \Lambda$ is the coulomb logarithm (≈ 10) and δ_T is a tabulated function²⁸ of Z . We use Eq. [35a] for T_e in the case $\tau > \tau_1$ and take the temperature gradient to exist over the laser spot radius, $\nabla T = 2T_e / D_s$ to find

$$Q = 1.78 \times 10^4 A^{7/16} f(Z) (I \lambda \sqrt{\tau})^{7/4} / D_s \quad \text{W/cm}^2. \quad [43]$$

The function $f(Z) = \delta_T Z^{13/8} / (Z+1)^{35/16}$ varies only slightly from 0.049 to 0.18 as Z varies from 1 to 16, decreasing again to a value 0.073 at $Z=100$. Therefore, a good approximation for the minimum laser spot size D_s such that $Q < I$ when $\tau > \tau_1$ is:

$$D_s > 1500 A^{7/16} I^{3/4} \lambda^{7/4} \tau^{7/8} \quad \text{cm.} \quad [44]$$

The limit given by Eq. [44] is most severe where A and $(I \lambda \sqrt{\tau})$ are large and D_s is small. However, for the aluminum data we quote ($A=27$ being a worst case), it is not serious for KrF lasers [$\tau = 22$ ns, $I = 10$ GW/cm², $D_s > 3.5$ μm], nor even for very long-

pulse, Nd lasers [$\tau = 1.5$ ms and $I = 3$ MW/cm², $D_s > 1.7$ mm], and marginally acceptable for laser fusion conditions [$\lambda = 1.06$ μ m, $\tau = 1$ ns, $I = 10$ TW/cm², $D_s > 500$ μ m].

Only in the case of short-pulse CO₂ lasers with small targets, e.g., the OPL laser where $\tau = 700$ ns, $I = 700$ MW/cm² and we require $D_s > 7$ mm, does a problem appear.

However, a further consideration governs the dimensionality of heat transfer in this problem. This is the question of whether x_0 , the distance which separates the target ablation surface (where heat is deposited) from the region near the critical density (where heat is generated) is much smaller than the interaction region transverse dimension D_s . If this is so, heat is demonstrably transmitted preferentially toward the target in the pattern in which laser light is deposited near the critical surface, rather than being smoothed out by transverse thermal gradients. The Eq. [5] discussion shows that this is the case, even for the OPL laser experiments.

This result is possible because Eq. [44] tends to overestimate thermal conduction, ignoring flux limitation²¹ and inhibition by magnetic fields.

A CO₂ laser fusion data point is the only instance we discuss in which $x_0 \gg D_s$ and Eq. [44] predicts significant transverse thermal conduction. This point is, however, acknowledged to be anomalous in our data comparison discussion.

We conclude that, in many cases, Eq. [6] adequately describes dimensionality limits.

A second question which may not be ignored in general concerns the effect of nonuniform illumination on large targets.

Since practical laser focal distributions have "wings" which extend, at some intensity, to large radius, a situation in which the target is large compared to the central peak of this distribution invites errors in determining intensity and pressure, unless intensity falls sufficiently rapidly with radius, or the illumination area is limited.

To see how fast intensity must fall for meaningful experimental results, we assume a planar target upon which falls a modified Lorentzian intensity distribution

$$I(r)/I_0 = [1+c(r/w)^2]^{-q/2} \quad [45]$$

where $c = [2^{2/q} - 1]$ [46]

and w is the FWHM intensity radius of the distribution. The case $q \leq 2$ is nonphysical, implying infinite beam power. We assume a uniform-intensity pulse.

We also assume that mechanical coupling varies with intensity as predicted by Eq. [31a], and ceases when $I < I_p$:

$$\begin{aligned} C_m/C_{m0} &= (I_p/I)^{1/4} , & I \geq I_p \\ &= 0, & I < I_p . \end{aligned} \quad [47]$$

We take the interaction as ceasing at the radial coordinate r_p where plasma formation begins. Then, with $x = (r/w)$, $u = [1+cx^2]^{1/2}$ and

$$x_p = \{[(I_0/I_p)^{2/q} - 1]/c\}^{1/2} \quad [48]$$

we have $p(r,t) = C_m I = C_{m0}(t) I^{3/4} I_p^{1/4} = I_0/(u^{3q/4} u_p^{1/4})$ dyne/cm² . [49]

The delivered impulse J is then

$$J = (2\pi w^2 I_0/u_p^{1/4}) \int_0^\tau dt t C_{m0}(t) \int_0^{x_p} dx x/u^{3q/4} . \quad [50]$$

Denoting by J_1 the impulse generated within the radius $r=w$, and by J_2 that generated within $r=w_p$ on the target (infinity for practical purposes), the ratio J_1/J_2 is given by:

$$J_1/J_2 = \left[\int_0^1 dx x/u^{3q/4} / \int_0^{x_p} dx x/u^{3q/4} \right] \quad [51]$$

$$= (2^a - 1) / [(I_0/I_p)^a - 1]$$

where $a = (2/q - 3/4)$.

Table IV shows how the behavior predicted by Eq. [47] depends on the radial index q of the beam distribution on target for the case $(I_0/I_p) = 1000$. Also tabulated is the ratio W_1/W_2 for the laser energy contained within $r=w$, for comparison. Note that beam intensity must drop off at least as fast as $1/r^4$ for 19% of the impulse to be generated within the FWHM of the incident beam distribution, since impulse is generated with

increasingly large C_m out to $r_p = 8.6$ w in this case.

Mutually consistent numbers for the Sprite data point discussed above (see Fig. 6) are: $(I_o/I_p) = 496$, $x_p = 4.5$, $q = 7.75$, $J_1/J_2 = 30\%$, and $W_1/W_2 = 41\%$, indicating reasonably good beam quality in this laser system.

To demonstrate that the beam modeling in this section is not too far from reality, Figure 8 shows data obtained from the Los Alamos Aurora 5-kJ KrF laser system, when it was configured for laser impulse measurements. This data is included here because it is our only example of a quantitative measurement of the complete distribution $I(r)$. The data was obtained via a linear fluorescer and vidicon camera at the diagnostic beam focus. The Figure shows that the measured intensity distribution closely approximates the modified Lorentzian model out to the instrumental detection limit at $x = 60$. Analysis of this data showed beam intensity varying only slightly faster than $1/r^2$ [$q = 2.04$], and gave $I_o/I_p = 2470$, $x_p = 47$, $J_1/J_2 = 0.034$, and $W_1/W_2 = 0.095$.

Our conclusion from this discussion is that adequate control of high-energy-laser beam spacial profiles for small-spot impulse measurements is achievable.

On the other hand, errors due to transverse propagation of the pressure pulse across the target during the laser pulse can obviously be very severe when $c_a\tau \gg D$.

These features together suggest artificially limiting the area over which pressure can be generated on the target to a small multiple of the laser spot diameter.

IMPULSE MEASUREMENT

Two types of impulse-measuring device were used in these experiments. The first was conventional in design and had certain advantages for measuring large impulses, while the second device was designed for simplicity and high accuracy in measuring very small impulses expected in laboratory-scale laser experiments. In practice, every effort was made to make the illuminated and physical target areas identical.

Figure 9 illustrates the impulse gauge used for Mjöllnir, Gemini, and Sprite experiments, where delivered impulse was as large as 30,000 dyne-sec. The gauge pictured is a free-sliding displacement transducer, upon which the target was mounted. Its voltage output as a function of time was computer-corrected for friction-induced deceleration and differentiated to obtain velocity and thus momentum of the mobile

portion that holds the target. Minimum impulse that could be measured with good accuracy was about 20 dyne-sec; accuracy in the 10^3 - 10^4 dyne-sec range was about 2%. The gauge was calibrated by impact of a test object with accurately known momentum. With this gauge, each change in illumination area required, in principle, installation of a different-size target mounting head to properly control illumination uniformity. At times, this was impractical, so there is more scatter in the incident intensity we measured with high-energy lasers than with the improved technique we used in low-energy laser experiments.

In the OPL and EMG experiments, it was necessary to measure impulses as small as 0.01 dyne-sec with good accuracy, three orders of magnitude below the capability of the Figure 9 gauge. For these experiments, we redesigned the impulse measurement system, paying special attention to illumination area limitation.

In the new technique, small spherical targets were levitated in vacuum by the impulse produced when the focused laser pulse was incident from below the target. The delivered momentum was determined from measured levitation height h and target mass m via the relationship

$$J = \sqrt{2gh} \ m \quad \text{dyne-sec.} \quad [52]$$

The target support (see Fig. 10) was a circular knife-edge which closely contacted the target surface prior to launch. By appropriate choice of target mass for each shot, we could maintain a maximum levitation height of about 10 cm, so that initial target velocity was $1.4 \mu\text{m}/\mu\text{s}$ or less, ensuring close contact between the target and its support iris during ablation pressure pulses as long as $1 \mu\text{s}$.

In this way, the target area over which both illumination and ablation pressure were applied could be carefully defined. Good electrical contact between the target and the grounded launch platform via the photoplasma was also ensured for a time much longer than the interval for electric field generation by charge separation, eliminating electrostatic effects on target motion.

Further advantages of the levitation method for impulse measurement were simplicity, good accuracy (2%), and self-calibration, since target mass was always

chosen to be at least 100 times larger than the mass lost in the interaction.

Levitation height was measured by continuously illuminating the target and photographing its path against a fixed scale with an open-shutter camera, as shown in the Figure. Targets ranging from 800 μm to 3.2 mm diameter were used, with masses ranging from 1/2 mg to 30 mg, depending on expected laser energy, impulse coupling coefficient and mass loss. The supporting iris diameter varied from 200 μm to 2 mm.

Off-center illumination of the target in this technique alters the linear momentum imparted only if the resulting target peripheral rotation velocity is as large as the linear velocity at launch, causing mechanical reaction of the target against its support. It can be shown that this condition will not occur if eccentricity of the illumination centroid is less than 1/4 of the target radius. For targets as small as 200 μm diameter, this condition required moderate care; parabolic flight paths such as shown in Fig. 10 were actually a signal to discard misaligned shots.

The major source of error in experiments employing this technique were associated with accurate measurement of incident intensity, rather than of momentum.

For targets in vacuum, this technique could also be applied to the measurement of very large target momenta.

EXPERIMENTAL DIMENSIONALITY

Among the Los Alamos data reported here, only the Mjölnir and OPL experiments were definitely two-dimensional (see Table III). However, within the accuracy of the C-N-K model, a comparison of Eq. [10] and $I/I_t [= (D_t/D_s)^2]$ from Table III shows that, even when $D_t/D_s = 20$, as in the worst-case OPL data, the effect on measured impulse predicted by C-N-K given by the $(D_s/D_t)^{-1/9}$ dependence is about a factor of 1.5.

Previous experience, physical reasoning and the C-N-K model agree in predicting increased coupling above the 1-D to 2-D transition. Physically, this effect arises from the laser absorption layer moving closer to the target as lateral expansion of the plume causes density to fall more quickly than in the 1-D case.

In fact, a comparison of aluminum target data generated by OPL ($D_t/D_s \geq 30$, data "e" in Fig. 11) with the trend line for the Gemini data ($D_t/D_s \geq 8$, data "g" in Fig. 11) shows vertical separation of the data by a factor of 1.5, in favor of OPL data.

Our conclusion from this discussion is that, when the ratio D_t/D_s is not very large and the target ablation pressure area is mechanically defined, impulse experiments done with small laser systems yield data which is quite useful for scaling purposes.

PROCEDURE FOR SELECTING OTHER DATA AND FOR DATA PLOTTING

It was necessary to include data from other laboratories in Figs. 11-13 in order to adequately represent the other extreme from our own in the quantity $(I\lambda\sqrt{\tau})$.

Certain general rules were used. Only data for $I > I_{\max}$ were recorded (for example, in ref. 5 aluminum data, $I > 10^8$ W/cm²), since our model is not intended for smaller intensities. This restriction barely admits ref. 36 data. Occasionally, very high-intensity points representing a dimensionality transition were deleted when their inclusion would confuse the slope of a data trend, e.g., in Sprite data above 10^{11} W/cm². Data with large scatter was not plotted when better data was available for the same material type in the same $(I\lambda\sqrt{\tau})$ range.

Only a small selection of the very important long-pulse data exists, so that some data obtained in non-ideal circumstances had to be used. In particular, the ref. 26 data was obtained in air rather than in vacuum, with necessarily large dimensionality effects at $\tau = 1.5$ ms. At the low intensities corresponding to I_{\max} for this data (about 3 MW/cm²), air ionization should be unimportant, and generated pressure should be similar to that found in vacuum. However, since $D_t/D_s \approx 9000$ and our experience with Mjöllnir data in air shows the strong effect of atmospheric tamping on the interaction above I_{\max} , we have used only the I_{\max} data point from ref. 26.

Table V summarizes the experimental conditions employed for other data quoted .

On principle, the ref. 38 data should not be included here, since this is the only case in which $\tau_1 \gg \tau$ (see Table I). However, fortuitously, the data agrees with the empirical trend line for aluminum (Fig. 11).

Ref. 5 data is consistently 50 to 100% above the empirical trend, both with aluminum and C-H targets, suggesting systematic errors in determining impulse or intensity, and so is not included in this comparison despite its otherwise high quality.

DATA MODELING

___Figures 11-13 show that a representative sampling of existing vacuum impulse coupling data from 21 different experiments covering 7 orders of magnitude in the parameter $I\lambda\sqrt{\tau}$ agrees within a factor of 1.6 with an empirical trend:

$$C_m = b (I\lambda\sqrt{\tau})^n \quad [54]$$

For aluminum alloys (e.g., 2024, 6061), $b = 5.6$ and, for C-H materials, $b = 6.5$. For both material types, $n = -0.300 \pm 0.03$.

___Since the C-N-K model for $\tau_1 \gg \tau$ apparently predicts $n = -0.25$, we looked for ways to resolve this discrepancy.

It will be recalled that Eq. [31a] predicts a $\Psi^{9/16}$ -dependence for C_m . Since Ψ is obviously dependent on temperature and therefore upon $I\lambda\sqrt{\tau}$, we decided to develop a numerical Z-predictor based on the Saha equation⁴⁰ for Al and C, and to use this predictor to generate values for $\psi(I\lambda\sqrt{\tau})$, as inputs to Eq. [31a] during modeling of aluminum and of C-H data. We found that this could be done in an approximate way which did not grossly compromise the principle of simplicity in the overall model.

The Saha equation gives the degree of ionization for a plasma in thermal equilibrium as:

$$(N_i/N_{i-1})P_e = 2(U_i/U_{i-1})(2\pi m_e)^{3/2}[(kT)^{5/2}/h^3]\exp(-\chi_{i,i-1}/kT) \quad [55]$$

where N_i are the density of ions in the i th state of ionization, m_e , k and h are the electron mass, and the Boltzmann and Planck constants, U_i are the statistical partition functions for the ionization states, $P_e = n_e k T_e$ is the total electron pressure (dyne/cm²),

$$\text{and} \quad \chi_{i,i-1} = \Delta E_{i,i-1} - 7.0 \times 10^{-7} N_e^{1/3} i^{2/3} \quad [56]$$

is the energy difference between the i th and $(i-1)$ th ionization states corrected for merging of high-level spectrum lines. The assumption of thermal equilibrium is justified for all the data we consider.⁴¹

In our procedure, Eq.[35] is used to obtain a first estimate of T_e with $\Psi = \psi = 1$. The

Saha equation is then employed (using Eq. [34] for the required electron density input) to generate a population-density matrix of ionization states for the atom. This population-density matrix is then averaged to obtain an effective value for Z and Ψ or ψ . These values are returned to Eqs. [34] and [35] to find improved values for n_e and T_e , and the process repeated until convergence is obtained. The calculation is terminated if less than full ionization is predicted ($Z < 1$), a condition which would violate the assumptions of C-N-K. The "obscuration time" τ_1 [Eq. 29] is continuously computed, and a transition made to the critical-pressure regime when appropriate.

Our numerical Z-predictor was benchmarked against standard laser-fusion data from experiments^{42,43} with carbon at 3 and 120 eV and with aluminum at 200 eV, and calculations⁴⁴ of vacuum irradiation of aluminum. We found that the temperatures predicted by Eq. [35] were too high by about a factor of 2, but that, at a given temperature, our Saha predictor gave adequately accurate results for the ionization states. The temperature error arises from the neglect of higher-order details of material properties and of radiation transport in our model, in order to achieve simplicity.

Because Eq. [34] is not simply dependent upon $(I\lambda\sqrt{\tau})$, slightly different C-N-K predictions are obtained with different inputs for λ and τ in the low-to-moderate $(I\lambda\sqrt{\tau})$ range. The effect of T_e prediction errors is to give an excessive split between coupling predictions in this range.

To show the range of these model predictions for our data, Fig. 11 is reproduced in Fig. 12 with 5 model plots added, for aluminum atoms in a representative set of illumination conditions. These are: uv short pulses ("Turner", $\lambda = 248$ nm, $\tau = 22$ ns), mid-spectrum short pulses ("Arad", $\lambda = 1.06$ μ m, $\tau = 500$ ps), infrared long pulses ("Gemini", $\lambda = 10.6$ μ m, $\tau = 1.8$ μ s), and infrared short pulses ("Goldstone", $\lambda = 10.6$ μ m, $\tau = 1.1$ ns). In Fig. 13, carbon replaces aluminum in the model, with the substitution of the very interesting mid-spectrum long-pulse case ("Afanas'ev", $\lambda = 1.06$ μ m, $\tau = 1.5$ ms) in an otherwise similar set of cases.

DISCUSSION AND CONCLUSIONS

Our ψ -predictor modified the basic C-N-K estimate for C_m using $Z=1$ by as much as a factor of 3.5 for Al and 2.5 for C, for $\tau > \tau_1$ at low $(I\lambda\sqrt{\tau})$. This difference qualitatively

reflects the far lower electron density generated by long-pulse infrared lasers relative to short-pulse uv lasers at the same $(I\lambda\sqrt{\tau})$, and the corresponding increase in the density of higher ionization states predicted by the Saha equation. This feature arises because the primary parametric dependence for electron density in the model (Eq. [34a]) is $n_e \propto I / (I\lambda\sqrt{\tau})^{3/4}$; holding $(I\lambda\sqrt{\tau})$ constant while increasing $\lambda\sqrt{\tau}$ causes a proportional decrease in n_e , more than two orders of magnitude in the transition from KrF short pulses to infrared long pulses..

___The notable step-wise changes in the Figure 12 and 13 impulse predictions arise from the ionization of successive electron shells in aluminum and carbon atoms. Each transition is quite sudden because of the nonlinear coupling expressed in Eqs. [34a], [35a], and [50] between Z and $(I\lambda\sqrt{\tau})$. Heuristically, increasing $(\lambda\sqrt{\tau})$ increases T_e , but decreases n_e , generating higher Z via Eq. [50], which further depresses n_e via Eq. [34a]. This instability is not present when $\tau_1 > \tau$, e.g., in the "Goldstone" plot in Fig. 12.

Average Z is not important at moderate-to-high $(I\lambda\sqrt{\tau})$ values because Z is maximized, $\Psi \approx 1$, and, to this extent, all C_m plots for the same regime converge.

As a general statement, the inclusion of intensity-dependent ionization effects in this simple scaling model allows the prediction of impulse coupling results obtained in 21 different laser-target interaction experiments in vacuum to within a factor of 2 or better. In the case of C-H-type target materials, the agreement between prediction and experiment is usually better than 50% for a representative selection of data.

This is true over 7 orders of magnitude in laser intensity from 3 MW/cm² to 70 TW/cm², for pulse durations covering 6 orders of magnitude from 1.5 ms to 500 ps, and incident laser energies from 100 mJ to 2.5 kJ, even with modest departures from strict one-dimensionality.

The empirical trend (Eq. [54]) follows data for which $\tau > \tau_1$ equally well in a numerical sense, but without providing an indication of the physical reasons for departure from the trend in a specific case.

These results indicate the possibility of very simple scaling estimates of pressure and coupling in vacuum, for intensities above the plasma threshold, that are accurate within 50% for many types of pulsed laser-target interactions.

The magnitude of the disagreement between data and theory is surprising in its

smallness, considering the simplistic assumptions under which C-N-K was derived.

In fact, we have sought in this paper a simple enough model that the interaction physics is not obscured; clearly, more sophisticated but less general treatments are available, when better accuracy of impulse prediction is required. Such treatments will usually be necessary when target material properties cannot be ignored, as in the case of volume-absorbing, semi-opaque targets.

Given proper delimitation of the physical area over which laser-target interaction can occur, data from small lasers has been shown to be nearly as useful as that from large laser systems. Certainly, the dimensionality correction between the two does not have to be large. Further, small-laser data can be obtained relatively rapidly and accurately.

ACKNOWLEDGMENTS

The authors are grateful to Dr. Ray Kidder of Lawrence Livermore Laboratory for useful discussions, and, at Los Alamos, to Dr. Joe Figueira for his support, and to Chloe Muhs, Lois Schneider, Evelyn Cone, Dorothy Hatch, Maida Trujillo and Beverly Wallwork for their patient help with the manuscript.

TABLE I. Transition time τ_1 (s) vs. intensity I for several wavelengths in a hydrogenic plasma ($A=Z=1$)

I (W/cm ²)	$\lambda = (\mu\text{m}):$	0.248	0.694	1.06	3.0	10.6
10^7		2.2×10^{-15}	6.7×10^{-14}	2.7×10^{-13}	8.8×10^{-12}	5.9×10^{-10}
10^9		4.7×10^{-14}	1.4×10^{-12}	5.9×10^{-12}	1.9×10^{-10}	1.3×10^{-8}
10^{11}		1.0×10^{-12}	3.1×10^{-11}	1.3×10^{-10}	4.1×10^{-9}	2.7×10^{-7}
10^{13}		2.2×10^{-11}	6.7×10^{-10}	2.7×10^{-9}	8.8×10^{-8}	5.9×10^{-6}
10^{15}		4.7×10^{-10}	1.4×10^{-8}	5.9×10^{-8}	1.9×10^{-6}	1.3×10^{-4}

TABLE II. Expressions for laser-target interaction variables vs. A , Z , $\psi = A/2Z$, $\Psi = A/2[Z^2(Z+1)]^{1/3}$, λ (cm), τ (s) and I (W/cm²) for a square pulse

Quantity	(a) Subcritical regime, $\tau > \tau_1$		(b) Critical regime, $\tau \leq \tau_1$	Units	Eq.
Ablation pressure $p_a =$	$5.83 A^{-1/8} \Psi^{9/16} I^{3/4} (\lambda \sqrt{\tau})^{-1/4}$	\leq	$p_c = 15.6 \psi^{1/3} (I/\lambda)^{2/3}$	dyne/cm ²	[30]
Coupling coefficient $C_m = p_a I =$	$5.83 A^{-1/8} \Psi^{9/16} (I \lambda \sqrt{\tau})^{-1/4}$	\leq	$C_{mc} = 15.6 (\psi / I \lambda^2)^{1/3}$	dyne/W	[31]
Sound speed $c_a = [I / (\xi \rho_a)]^{1/3} =$	$1.37 \times 10^6 A^{1/8} \Psi^{-9/16} (I \lambda \sqrt{\tau})^{1/4}$	\geq	$c_{ac} = 5.12 \times 10^5 (I \lambda^2 / \psi)^{1/3}$	cm/s	[32]
Mass ablation rate $\dot{m} = \rho_a c_a =$	$2.66 \times 10^{-6} A^{-1/4} \Psi^{9/8} (I / \lambda \sqrt{\tau})^{1/2}$	\leq	$\dot{m}_c = 1.91 \times 10^{-5} I^{1/3} \psi^{2/3} \lambda^{-4/3}$	g cm ⁻² s ⁻¹	[33]
Electron density $n_e = \rho_a Z / (A m_p) =$	$3.59 \times 10^{11} A^{5/16} Z^{-1/8} (Z+1)^{-9/16} I^{1/4} \tau^{-3/8} \lambda^{-3/4}$	\leq	$n_{ec} = 1.115 \times 10^{13} \lambda^{-2}$	cm ⁻³	[34]
Electron temperature $T_e = [A m_p / \gamma k (Z+1)] c_a^2 =$	$2.98 \times 10^4 A^{1/8} (Z+1)^{-5/8} Z^{3/4} (I \lambda \sqrt{\tau})^{1/2}$	\geq	$T_{ec} = 3.79 \times 10^3 \psi^{1/3} I^{2/3} \lambda^{4/3}$	K	[35]
Impulse flux $\sigma = p_a \tau =$	$5.83 A^{-1/8} \Psi^{9/16} I^{3/4} \tau^{7/8} \lambda^{-1/4}$	\geq	$\sigma_c = 15.6 \psi^{1/3} (I/\lambda)^{2/3} \tau$	dyne-sec/cm ² or taps	[36]
Energy coupling coefficient $\eta = W_m / W_L = 10^{-7} \sigma^2 / (2 \mu I \tau) =$	$1.70 \times 10^{-6} A^{-1/4} \Psi^{9/8} \mu^{-1} I^{1/2} \lambda^{-1/2} \tau^{3/4}$	\geq	$\eta_c = 1.22 \times 10^{-5} \psi^{2/3} I^{1/3} \lambda^{-4/3} \tau \mu^{-1}$	---	[37]
Absorption length $L = c_a \tau =$	$1.37 \times 10^6 A^{1/8} \Psi^{-9/16} (I \lambda)^{1/4} \tau^{9/8}$	\geq	$L_c = 5.12 \times 10^5 (I \lambda^2 / \psi)^{1/3} \tau$	cm	[38]

TABLE III: Laser Facility Parameters for Los Alamos Coupling Data Reported Here

Facility, Type (location)	Dates	Wavelength	Maximum Target Energy	Pulselength (FWHM)	Target Spot Diameter D_S	Target Intensity Range, this Data, (W/cm ²)	Approximate Minimum 1-D Spot Dia. $D_t = 2c_a t$	Repetition Rate (per hour)	Notes
1. Mjollnir, HF (Kirtland AFB)	1983	2.7-3.4 μm	2.5 kJ	1.8 μs	1-3 cm	$2 \times 10^8 - 2 \times 10^9$	7 cm	0.3	1,4,5a, 6b,8b,9a
2. Gemini, CO ₂ (Los Alamos)	1984	10.59 μm	2.0 kJ	1.8 μs or 700 ns	1-7 cm	$3 \times 10^7 - 7 \times 10^8$	8 cm	4	(1,8b) or (2,3,8a,10), 5a,6c,9a
3. Sprite, KrF (Rutherford,UK)	1984	248 nm	100 J	40 ns	0.1-2.5 cm	$3 \times 10^8 - 3 \times 10^{11}$	0.2 cm	4	1,3,5a,6a, 8a,9a,10,11
4. Optical Physics Lab(Los Alamos)	1985	10.59 μm	5 J	700 ns	1.4 mm	$7 \times 10^7 - 7 \times 10^8$	30 mm	20	2,5b,6b,7, 8a,9b,10,11
5. Lambda-Physik EMG-150 facility (Los Alamos)	1986	248 nm	100 mJ	22 ns	0.1 mm	$7 \times 10^8 - 1 \times 10^{10}$	0.4 mm	20	2,3,5c,6a,7, 8a,9b,10

Notes:

- | | | |
|--------------------------------------|------------------------------------|---|
| 1. Unstable resonator | 6. Dimensionality: | 9a. Mechanical impulse gage |
| 2. Oscillator/amplifier | a. largely 1-D | 9b. Impulse measured by target levitation |
| 3. Injection-controlled beam quality | b. definitely 2-D | 10. Well-controlled temporal pulse shape |
| 4. Multiline spectrum | c. transition | 11. Well-controlled spatial pulse shape |
| 5. Background pressure: | 7. Attenuators used to vary energy | |
| a. $<10^{-4}$ torr | 8a. Linear polarization | |
| b. ≤ 10 mtorr | 8b. Random polarization | |
| c. ≤ 200 mtorr | | |

TABLE IV: Fraction of Total Impulse and Beam Energy within FWHM Radius vs. Radial Intensity Index q and Plasma Threshold Radius $x_p = (r_p/w)$ when $I_0/I_p = 1000$

$q \equiv$	$x_p \equiv$	Impulse Ratio $\underline{J}_1/\underline{J}_2 \equiv$	Energy Ratio $\underline{W}_1/\underline{W}_2 \equiv$
$2+\delta$	31.61	0.041	0.100
3	12.98	0.128	0.229
4	8.60	0.194	0.302
6	5.88	0.266	0.374
8	4.94	0.302	0.408
10	4.48	0.324	0.427
12	4.20	0.339	0.440
∞	3.16	0.408	0.500

TABLE V: Experiment Parameters for Other Data Quoted in Figs. 11-13

Source (Reference)	Wavelength	Maximum Target Energy	Pulselength (FWHM)	Target Spot Diameter	Target Intensity Range (W/cm ²)	Approximate Minimum 1-D Spot Dia. $D_t \equiv 2c_a\tau$	Notes
1. Afanas'ev ^a	1.06 μm	800J	1.5 ms	4 mm	3.5×10^6	36 m	1, 6b
2. Gregg&Thomas ^b	694 nm	1.5J	7.5ns	660 μm	5×10^8 - 4×10^{10}	400 μm	2, 6a
3. Rudder ^c	1.06 μm	100J	1 μs ,5 μs	6 mm	3×10^8 , 6×10^7	150 mm	3, 6b
4. Arad, <u>et al.</u> ^d	1.06 μm	15J	500 ps	200 μm	5×10^{12} - 9×10^{13}	400 μm	4, 6a
5. Goldstone, <u>et al.</u> ^e	10.6 μm	150J	1.1 ns	600 μm	4×10^{13} , 7×10^{13}	1100 μm	5, 6b
6. Grun, <u>et al.</u> ^f	1.05 μm	150J	3-5ns	1 mm	4×10^{11} - 3×10^{13}	2 mm	6a

Notes:

- | | | |
|---|---|-------------|
| 1. $D_t/D_s = 7000$, atmospheric target environment | a | see Ref. 26 |
| 2. Some question concerning accuracy of intensity measurement. | b | see Ref. 5 |
| 3. Only highest intensity points quoted at $I=I_{\text{max}}$ | c | see Ref. 36 |
| 4. Data for 25, 50 and 75- μm thick aluminum foils only. | d | see Ref. 37 |
| 5. For this data only, $\tau \ll \tau_1$ (Table I) | e | see Ref. 38 |
| 6. Dimensionality: | f | see Ref. 39 |
| a. largely 1-D | | |
| b. definitely 2-D | | |

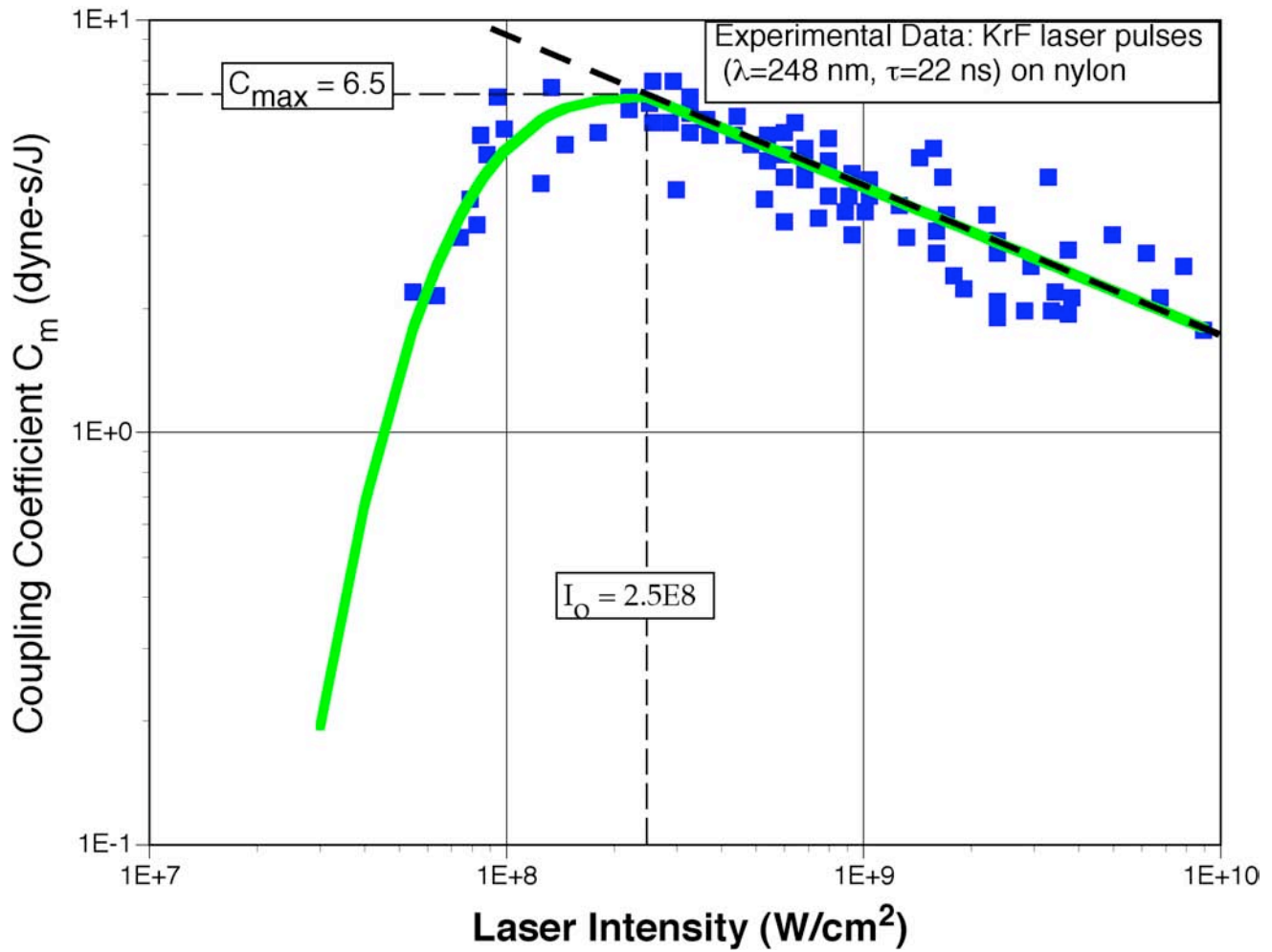


FIG. 1. Measured behavior of KrF laser mechanical coupling to nylon ($\lambda = 248$ nm, $\tau = 22$ ns, $I_{\max} = 10^8$ W/cm²). Solid line is a least-squares fit to data points at intensities greater than I_{\max} . Standard deviation of the spread of the points from the best fit line is 0.0782.

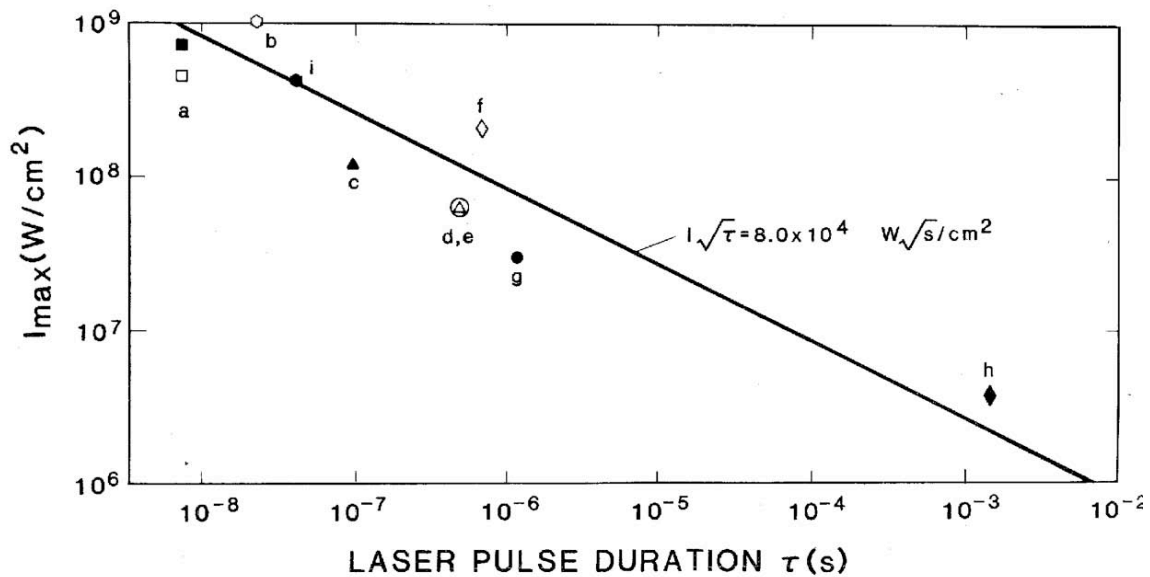


FIG.2. A survey of reported maximum coupling intensity I_{\max} at several wavelengths on aluminum and other metals. (a): D. W. Gregg and S. J. Thomas, *J. Appl. Phys.*, 37, 2787 (1966), 7.5 ns, 694 nm; (solid square): Be, (open square): Al. (b): T. Turner, C. R. Phipps, Jr., L. C. Haynes, and G. K. Anderson, unpublished, 248 nm, Al. (Los Alamos work) (c): I. Ursu, I. Apostol, D. Barbulescu, I. N. Mihailescu, and M. Moldovan, *Opt. Comm.*, 39, 180 (1981), 100 ns ("spike" portion of pulse), 10.6 μm , stainless steel. (d): D. I. Rosen, D. E. Hastings, and G. M. Weyl, *J. Appl. Phys.*, 53, 5882 (1982), 0.5 μs , 350 nm, 0.5 μs , 350 nm, Ti6Al4V alloy. (e): D. I. Rosen, J. Mitteldorf, G. Kothandaraman, A. N. Pirri, and E. R. Pugh, *J. Appl. Phys.*, 53, 3190 (1982), 2024 Al. (f): C. R. Phipps, Jr., and R. F. Harrison, unpublished, 700 ns, 10.6 μm , Al. (g): C. Duzy, J. A. Woodroffe, J. C. Hsia, and A. Ballantyne, *Appl. Phys. Lett.*, 37, 542 (1980), 1.2 μs , 350 nm, Al. (h): Yu. V. Afanas'ev, N. G. Basov, O. N. Krokhin, N. V. Morachevskii, and G. V. Sklizkov, *Zhurnal Tekn. Fiz.* 39, 894 (1969) [*Sov. Phys. Tech. Phys.* 14, 669 (1969)], 1.5 ms, 1.06 μm , Al. (i): Phipps, et al. Sprite laser (UK), 37 ns, 248 nm, Al (unpublished)

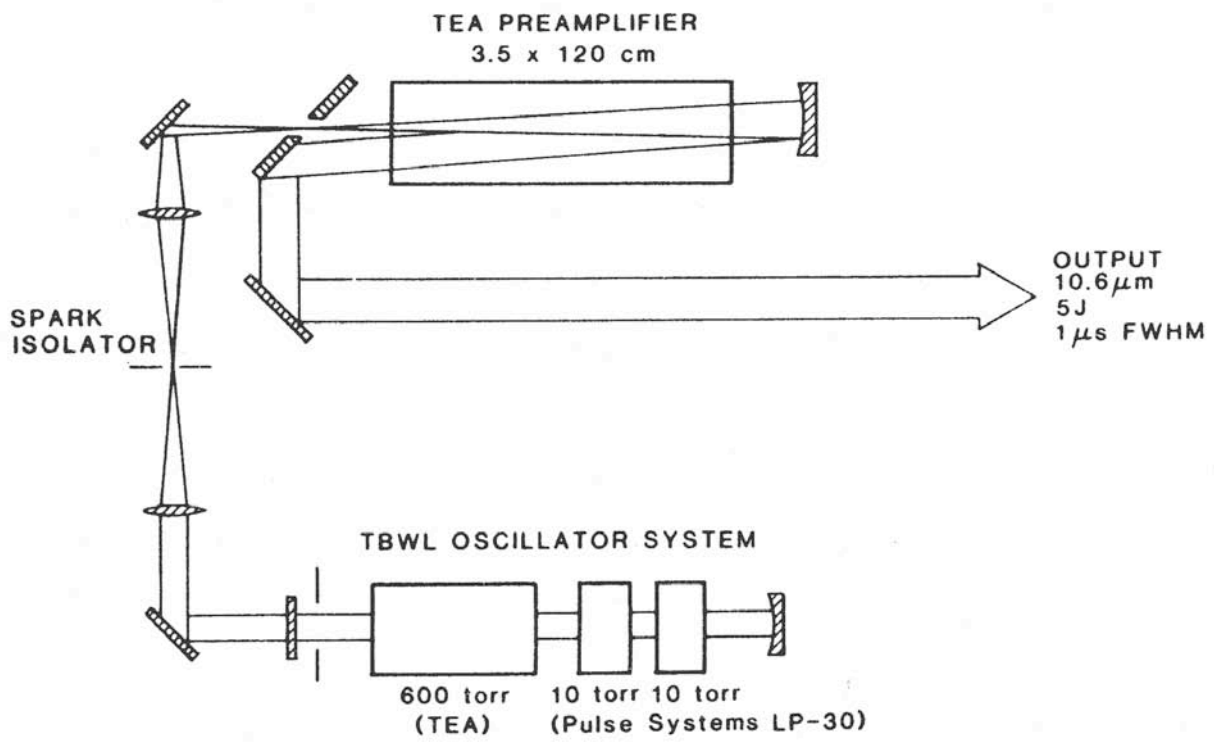


FIG 3. Block diagram for the Gemin MOPA front-end driver unit.

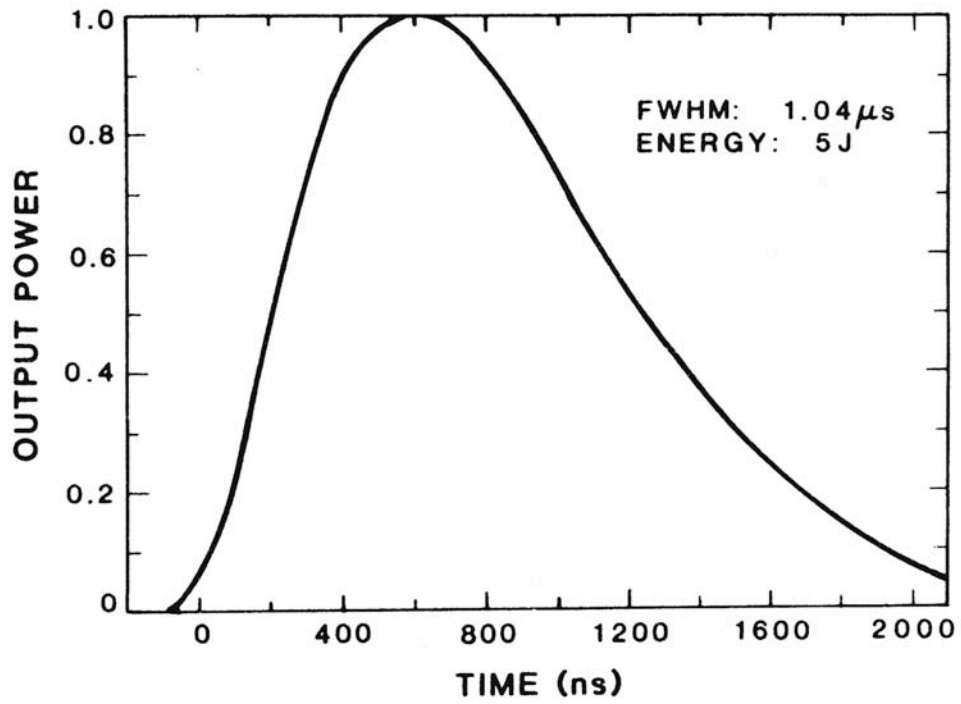


FIG 4. Output pulse shape for the Gemini MOPA front-end driver unit.

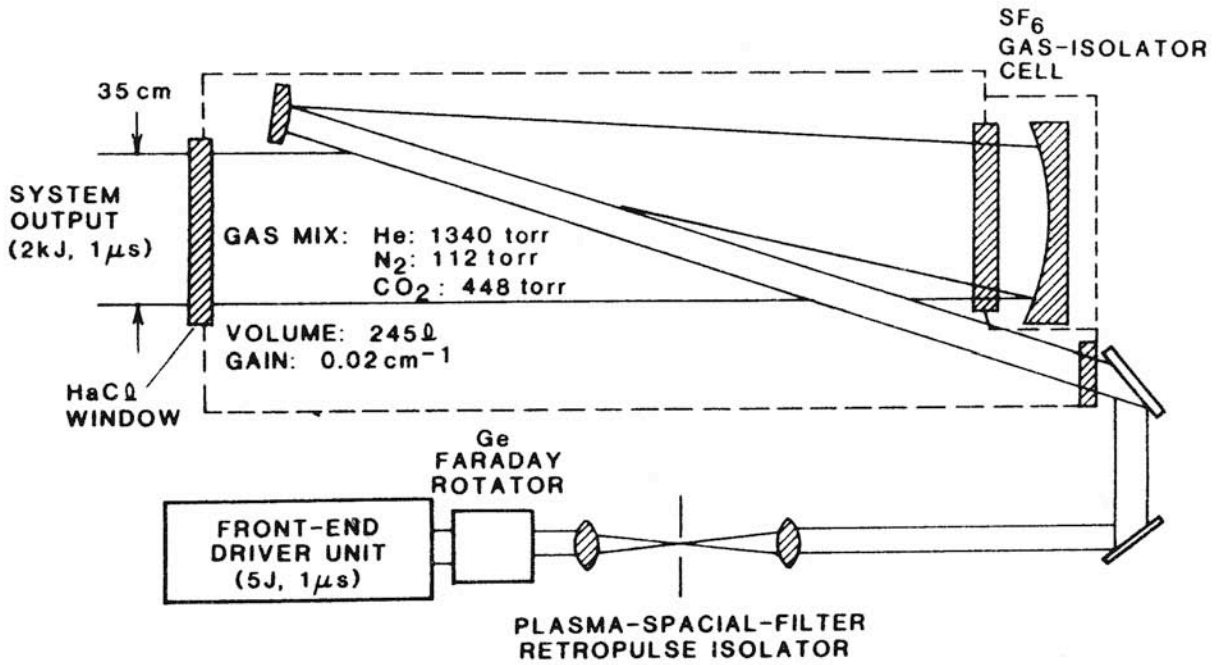


FIG 5. Block diagram for the Gemini MOPA



FIG 6. SEM photo of 6061-alloy aluminum target after irradiation by Sprite at $1.1 \times 10^{11} \text{ W/cm}^2$ at 25X magnification. Energy on target: 35J, central crater diameter 1mm, affected area diameter 4.5mm, $I_0/I_p = 500$, pulse duration 40ns.

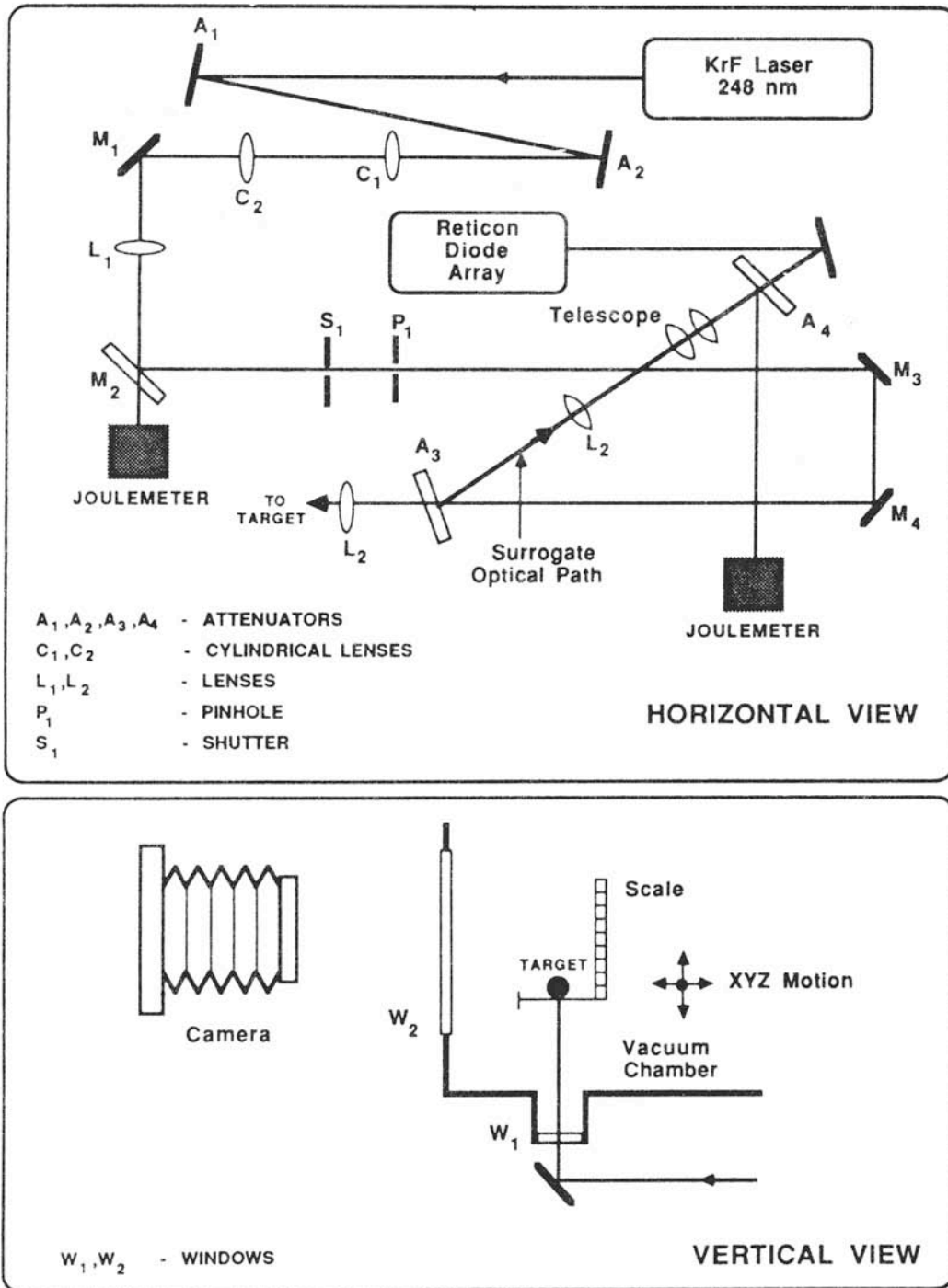


FIG 7. EMG-150 experimental setup.

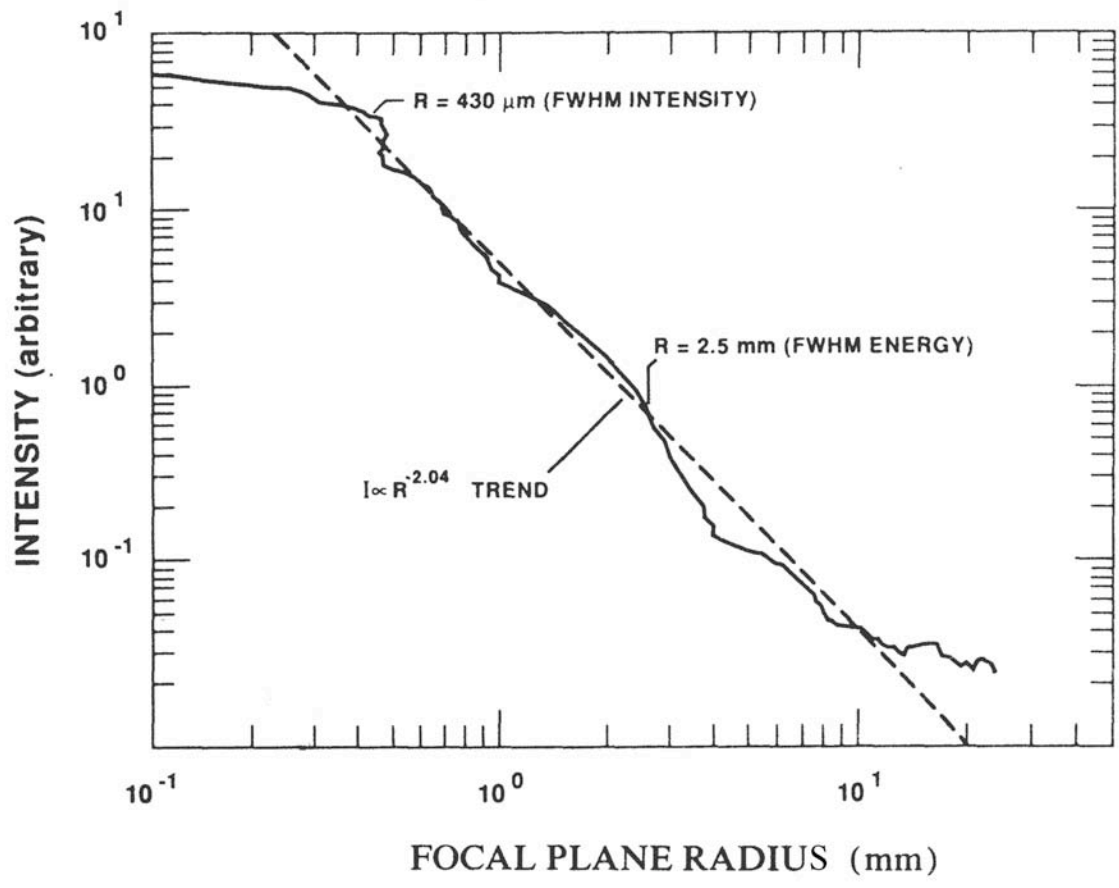


FIG 8. Radial intensity distribution data on the target plane for the Los Alamos Aurora 5kJ KrF system, showing $q = 2.04$.

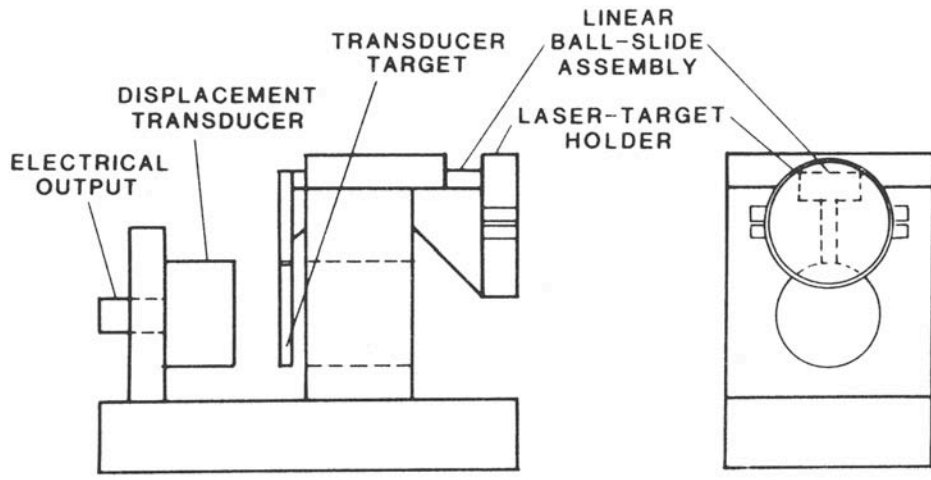


FIG 9. Electromechanical impulse gauge used for Mjöllnir, Gemini and Sprite experiments.

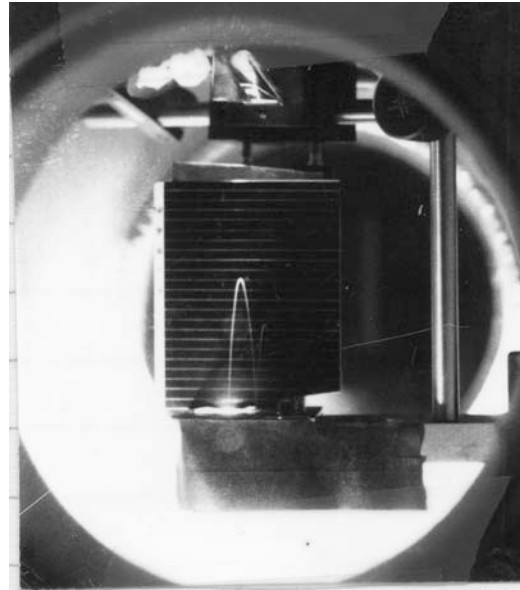
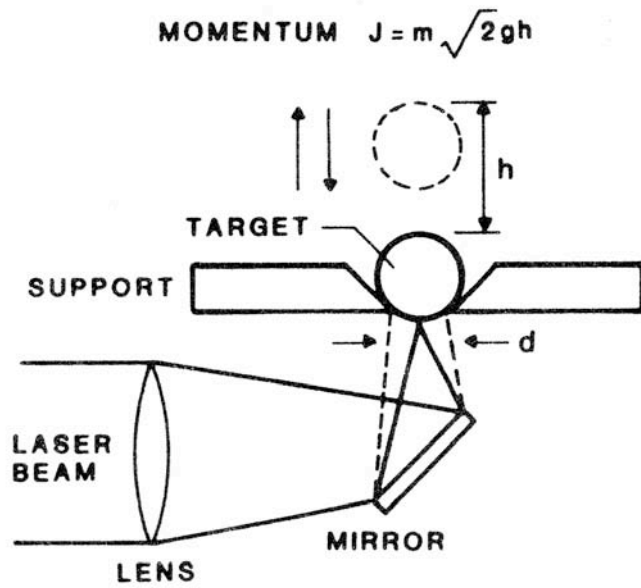


FIG 10. Levitation impulse gauge used for laboratory-scale impulse measurements with OPL and EMG lasers. Inset: actual open-shutter photograph of target motion during experiment.

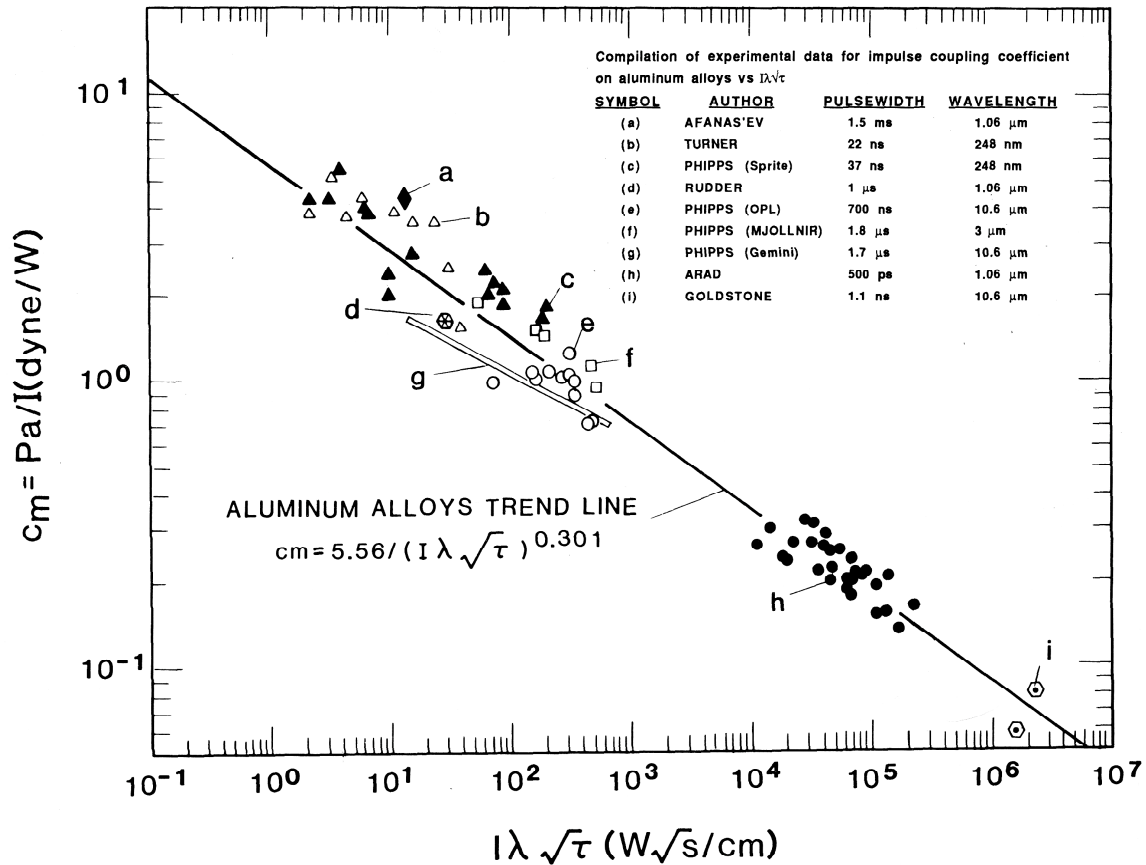


FIG 11. Compilation of experimental data for impulse coupling coefficient on aluminum alloys vs the parameter $(I\lambda\sqrt{\tau})$. (a): Afanas'ev, et al., *Zhurnal Tekn. Fiz.* **39**, 894 (1969) [*Sov. Phys. Tech. Phys.* **14**, 669 (1969)], **1.5 ms**, **1.06 μm** . (b): Turner, et al., *J. Appl. Phys.* **64**, 1083 (1988), **22 ns**, **248 nm**. (c): Phipps, et al., *J. Appl. Phys.* **64**, 1083 (1988), Sprite, **37 ns**, **248 nm**. (d): Rudder, U. S. Air Force Weapons Laboratory Report AFWL-TR-74-100 (1974)., **1 μs** , **1.06 μm** . (e): Phipps, et al., *J. Appl. Phys.* **64**, 1083 (1988), **700 ns**, **10.6 μm** . (f): Phipps, et al., *J. Appl. Phys.* **64**, 1083 (1988), Mjöllnir, **1.8 μs** , **3 μm** . (g): Phipps, et al., *J. Appl. Phys.* **64**, 1083 (1988), Gemini, **1.7 μs** , **10.6 μm** . (h): Arad, et al., *J. Appl. Phys.*, **50**, 6817 (1979), **500 ps**, **1.06 μm** . (i): Goldstone, et al., *Appl. Phys. Lett.*, **38**, 223 (1981), **1.1 ns**, **10.6 μm** . An empirical trend line is shown.

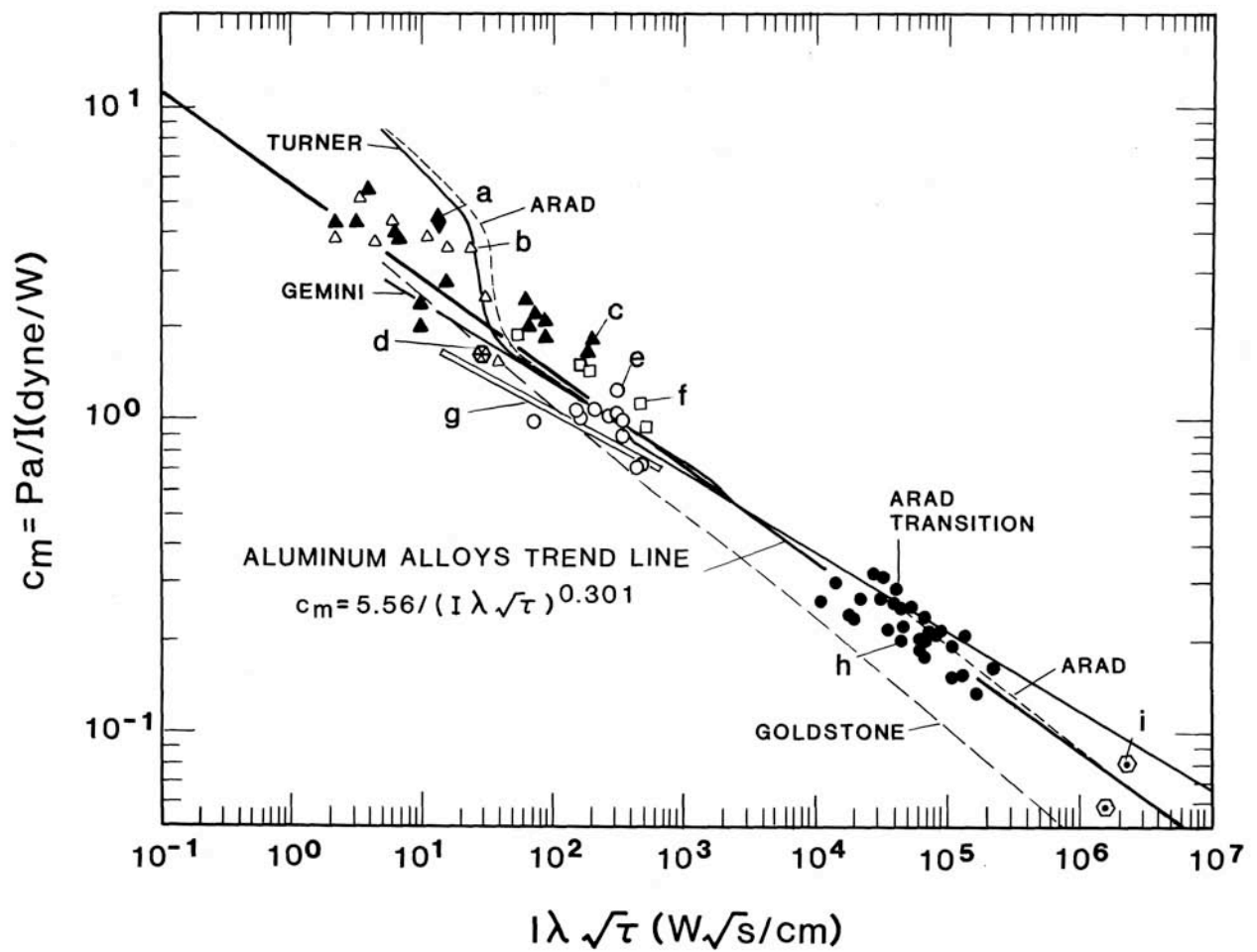


FIG 12. Figure 11 compilation with the addition of C-N-K model predictions of C_m based on four cases: UV short pulses (“Turner,” $\lambda = 248 \text{ nm}$, $\tau = 22\text{ns}$), midspectrum short pulses (“Arad,” $\lambda = 1.06\mu\text{m}$, $\tau = 500\text{ps}$), infrared long pulses (“Gemini,” $\lambda = 10.6 \mu\text{m}$, $\tau = 1.8 \mu\text{s}$), and infrared short pulses (“Goldstone,” $\lambda = 10.6 \mu\text{m}$, $\tau = 1.1\text{ns}$).

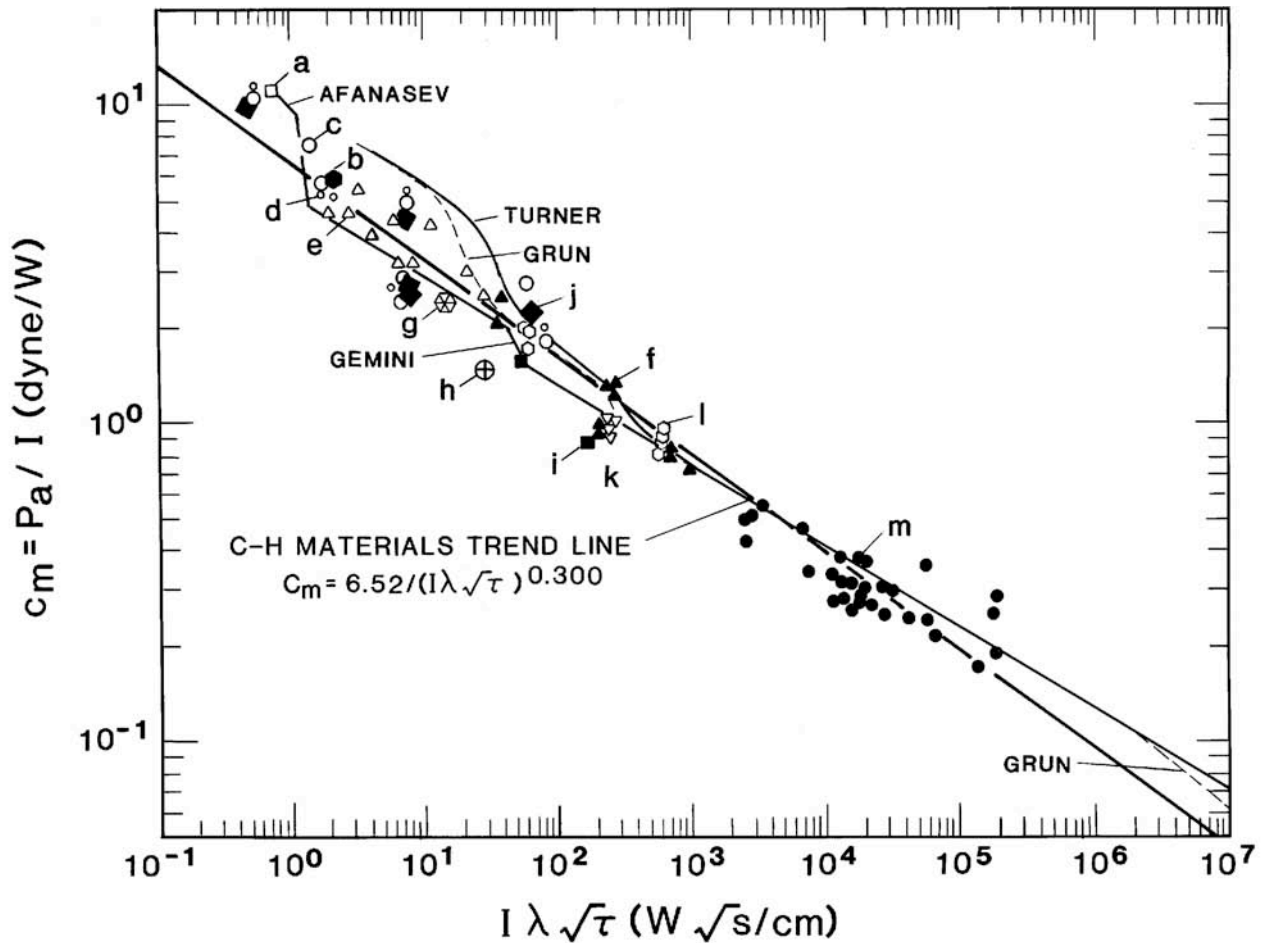


FIG 13.. Compilation of experimental data for impulse coupling coefficient on C-H materials vs. the parameter $(I\lambda\tau^{0.5})$, adapted from reference 60. (a): 1.5 ms, 1.06 μm on ebonite rubber. (b): 1.5 ms, 1.06 μm on carbon. (c): 37 ns, 248 nm, on silica phenolic. (d): 37 ns, 248 nm, on vamac rubber. (e): 248 nm, on buna-n rubber. (f): 1.7 μs , 10.6 μm on kevlar epoxy. (g): 5 μs , 1.06 μm , on Grafoil. (h): 1 μs , 1.06 μm , on Grafoil. (i): 1.7 μs , 10.6 μm on carbon. (j): 37 ns, 248 nm on carbon phenolic. (k): 1.7 μs , 10.6 μm on graphite epoxy. (l): 1.7 μs , 10.6 μm on carbon phenolic. (m): 4 ns, 1.05 μm , on C-H foils. Here the C-N-K model predictions of C_m are based on the following cases: UV short pulses (“Turner,” $\lambda = 248\text{ nm}$, $\tau = 22\text{ ns}$), midspectrum short pulses (“Grun,” $\lambda = 1.06\mu\text{m}$, $\tau = 5\text{ ns}$), midspectrum long pulses (“Afanas’ev,” $\lambda = 1.06\mu\text{m}$, $\tau = 1.5\text{ ms}$), and infrared long pulses (“Gemini,” $\lambda = 10.6\mu\text{m}$, $\tau = 1.8\mu\text{s}$).